International Journal of Rock Mechanics & Mining Sciences 46 (2009) 1124–1135

Contents lists available at ScienceDirect

International Journal of Rock Mechanics & Mining Sciences

journal homepage: www.elsevier.com/locate/ijrmms

Modeling Lac du Bonnet granite using a discrete element model

Yuannian Wang, Fulvio Tonon *

University of Texas at Austin, Department of Civil Engineering, Austin, TX 78712, USA

ARTICLE INFO

Article history:
Received 19 June 2008
Received in revised form
13 May 2009
Accepted 19 May 2009
Available online 25 June 2009

Keywords:
Discrete element model
Calibration
Micro parameter
Particle size
Crack propagation

ABSTRACT

A discrete element method code developed by the authors is used to model Lac du Bonnet granite in triaxial compression. The paper first presents the features of the model and the algorithms used to identify the micro deformability and strength parameters. With these identification algorithms, the model was calibrated to match experimental triaxial test data on Lac du Bonnet granite. With the calibrated model, investigation on failure evolution was then performed. The monitored evolution of the number and type of contact failures (micro cracks) reveals that at micro level tensile failures occur first, followed by mobilization of residual friction. Three distinct stages of stress–strain curve can be well identified by the accumulated number of contact failures and the mode of contact failures.

1. Introduction

The behavior of geomaterials, like intact rock, is often time complex, with a nonlinear failure envelope and a high ratio of uniaxial compression strength to tensile strength [1]. Currently, it is very difficult, if not impossible, to fully model this behavior, which has a complicated failure evolution process. Discrete element method (DEM) is a popular tool used in modeling rock behavior, because it can deal with the material failure naturally by modeling failure evolutionary process from micro crack to macro failure without any complex constitutive models.

DEM can be generally viewed [2] as a method that allows finite displacements and rotations of discrete bodies, and updates contacts automatically as the calculation progresses. The original application of DEM by Cundall and Strack [3] was to perform research into the behavior of granular material and blocky rock systems [4]. Then it has been extended to solid mechanics to investigate the failure process of bonded geomaterials, like intact rock [5,6] and concrete [7]. Nowadays, DEM is widely used in geomechanics from soil (particulate type) to intact rock (relatively continnum type), to rock masses (assemblies of blocks) with applications in many areas, such as rock engineering, soil mechanics, mining and petroleum engineering [3,8–13]. In modeling particulate materials, the element used in the model can be viewed as representing the true material particle. When modeling the behavior of intact rock, the elements used in the model do not represent the actual material particle size and the elements are bonded to each other with a specific strength.

While the method is versatile and attractive, it requires extensive calibration work. The calibration process in DEM includes parameter identification for both deformability and strength. Before modeling a specific case, the specimen should be prepared with specific micro parameters to be determined for a given packing so as to closely reproduce the specific macro material properties.

So far, there has been no satisfactory way to calibrate the DEM model in order to reproduce the complicated behavior of material like rock and deploy the versatility of DEM. Using sensitivity analysis, most of the researchers investigate the effect of one individual parameter (or a combined dimensionless parameter) while keeping other variables fixed, and then a general formula to determine micro-scale parameters based on specific macro material properties is determined [14,15]. Based on the authors' investigation, when identifying micro deformability parameters, the problem is relatively simple and sensitivity analysis can be applied. However, when identifying micro strength parameters, the problem involves micro crack propagation, and hence is more complicated, because the individual trend of one strength parameter may not be directly obtained by just fixing the values of all the other parameters since these parameters may not be independent. In PFC [16], for example, uniaxial compressive tests are used to reproduce the deformability behavior and the uniaxial compressive strength: as the authors note, "It should be noted that our current understanding of this calibration process is still incomplete—i.e., we still do not know how to construct a PFC material that reproduces a given strength envelope or one that reproduces a given ratio of unconfined compressive strength to Brazilian tensile strength …".

* Corresponding author. Tel.: +1 512 475 8196; fax: +1 512 471 6548.
E-mail address: tonon@mail.utexas.edu (F. Tonon).

1365-1609/$ - see front matter © 2009 Elsevier Ltd. All rights reserved.
doi:10.1016/j.ijrmms.2009.05.008

The paper first presents an outline of the authors' DEM code. Then it proceeds by introducing the simulation setups and the model calibration, in which an effective calibration technique to identify micro parameters has been successfully achieved with an optimization process, and a new membrane boundary to apply confining pressures for modeling triaxial tests is developed to overcome the drawbacks of conventional boundary conditions [6,16–18]. Finally, some important investigations on failure evolution during axial loading are performed to gain insight into the complex fracturing behavior of Lac du Bonnet granite.

2. Features and formulations of DEM code

A DEM algorithm has been implemented with the general features similar to other particle based programs while introducing some new features, such as concept of equilibrium contact distance. A very brief summary of the general features of DEM is given here.

2.1. Specimen preparation

The rock specimen is prepared as a random dense packing of sphere particles with different radii distributed according to a Gaussian distribution, in which the ratio of smallest radius over the largest radius is chosen as 1.6 in this paper. The dense packing assembly is achieved by using a modified radii expansion method described in Ref. [16]. Rigid walls are used to confine the space. In the method, sphere radii are first computed for a given number of particles and a desired porosity of packing. However, the porosity used for packing is not the physical porosity of a rock specimen because a coefficient of interaction range is used in the model to "cement" particles. In order to effectively place these sphere particles in a given domain, each sphere is shrunk to a smaller size by a certain percentage so that these shrunk sphere particles can be placed at random coordinates easily without any overlaps, because the available void space is relatively large. The spheres are then expanded to their originally calculated radii to obtain the desired porosity. Since this process may introduce large overlaps at contact, the assembly is cycled by using a simple DEM code to decrease the larger overlaps between particles and eventually reach equilibrium. This simple DEM code is similar to the DEM code presented in the paper except that particles are not bonded together. A Mohr–Coulomb contact model with relatively low friction is employed in the simple DEM code to make sure that particles can move easily with respect to one another.

The initial model is set up by using the packing assembly and by considering the initial state as "zero stress" state. This is achieved by introducing an "equilibrium distance" D_{eq}^{AB} between each pair of contact spheres A and B, which is equal to the distance between the centers of spheres A and B at the end of the packing (release of the lock-in stress). A coefficient of interaction range is introduced into the model to simulate materials other than simple granular materials, in particular those which involve a matrix [7]. A coefficient of interaction range of 1.3 is used in this work, which means that two particles are in contact if their center-to-center distance is less than 1.3 times of the summation of their radii.

As shown in Fig. 1, there are two scenarios in which particles are in contact and "equilibrium distance" is created. In one scenario, two particles are overlapped and "equilibrium distance" is less than the summation of their radii. While in the other scenario two particles are not physically in contact, but are still considered as a contact because of introducing interaction range, in which "equilibrium distance" is larger than the summation of their radii. For the former case, an "equilibrium distance" is to release the lock-in stress generated from packing, which is not appropriate for modeling. The equilibrium distance between particles, which are not in contact initially but may come into contact at some later stage in the simulation, is determined as the summation of the two radii multiplied by a coefficient of interaction range.

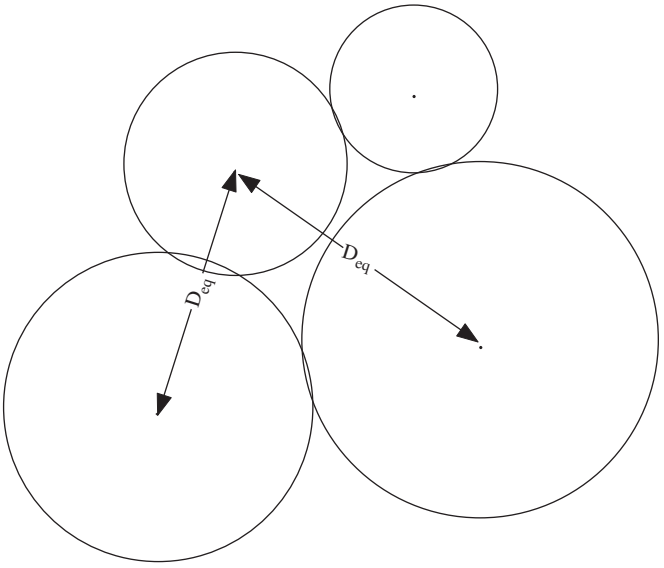

Fig. 1. Concept of equilibrium distance.

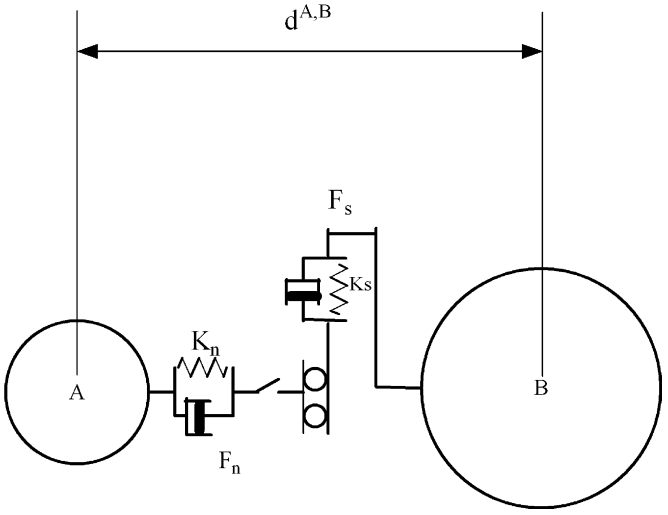

Fig. 2. Constitutive model of contact.

Fig. 2 shows the basic idea about the constitutive model implemented in the current model, in which the springs represent the elastic responses to normal and shear forces, the dashpots represent the damping effects of the material; and the slider element stands for the contact slide after shear failure.

2.2. Force–displacement law

The force–displacement law relates the relative displacement between two entities at a contact to the contact force acting on the entities. Here "force–displacement" is a general term including both force–displacement and moment–rotation. Only a brief description on force–displacement law is given here. More details can be referred to authors' related papers [19,20].

The relationship between contact forces and the relative displacements is assumed to be linear with the following interpretation. The contact forces consist of a normal component, $\vec{F}_n$, acting in the direction of the segment AB joining the two sphere centers, and a shear component, $\vec{F}_s$, acting in the plane perpendicular to AB at the point of contact, C. The force–displacement law relates these two force components to the corresponding components of the relative displacement via linear normal stiffness (K_n) and shear stiffness (K_s) at contact.

The normal force, $\vec{F}_n$, acting on sphere A is calculated as

$$\vec{F}_n = K_n(D_{eq}^{A,B} - d^{A,B})\,\vec{n}, \tag{1}$$

where $D_{eq}^{A,B}$ is equilibrium distance between the two spheres A and B which is set when the contact is initially created, $d^{A,B}$ is the current distance between each pair of contact spheres A and B, and $\vec{n}$ is the unit vector pointing from the center of sphere A to the center of sphere B. The contact is in tension when $d^{A,B} > D_{eq}^{A,B}$, and in compression when $d^{A,B} < D_{eq}^{A,B}$. The calculated new normal contact force is then added to the contribution of the resultant force and moment for both spheres. When tensile failure occurs at contact, the way to calculate the normal force will change, as described later in Section 2.3.

The shear contact force, $\vec{F}_s$, is determined from an updated shear displacement on the contact plane which is computed in an incremental fashion as

$$\vec{F}_s = -K_s \Delta\vec{U}_s, \tag{2}$$

where K_s is the shear stiffness of the contact, and $\Delta\vec{U}_s$ is incremental shear displacement. This new updated shear contact force is added to the resultant force and moment for both spheres. When a contact is formed, the shear displacement on the contact plane is initialized to zero. Each subsequent relative shear-displacement increment is added to the current value in a vector form, which will hence result in an increment in shear contact force. The motion of the contact must be taken into account during this procedure because the current shear displacement vector always lies on the contact plane, which moves with the spheres in the global coordinate system.

The moment applied to spheres A and B by the shear contact force, $\vec{F}_s$ can be calculated, respectively, as

$$\vec{M}_A = \vec{r}_{AC} \times \vec{F}_s,$$
$$\vec{M}_B = -\vec{r}_{BC} \times \vec{F}_s, \tag{3}$$

where $\vec{r}_{AC}$ and $\vec{r}_{BC}$ are radius vectors from sphere centers to the contact point, C, respectively.

2.3. Failure criteria

The strength criteria at contact used in the model comprise two parts: tensile failure and shear failure. These two kinds of failures jointly control the overall material strength. Tensile failure occurs when the magnitude of the contact normal force (in tension) is greater than the product of tensile strength, T, times the contact area, A_C, which is calculated as

$$A_C = \pi\left(\frac{R_A + R_B}{2}\right)^2, \tag{4}$$

where R_A and R_B are the radii of spheres A and B, respectively.

After tensile failure, the contact force suddenly drops down to zero and the contact is de-bonded in tension, which means that the tensile strength is zero after the tensile failure, in the meantime, the cohesion part of shear strength will also degrade to zero. In order to model the softening behavior of the material,

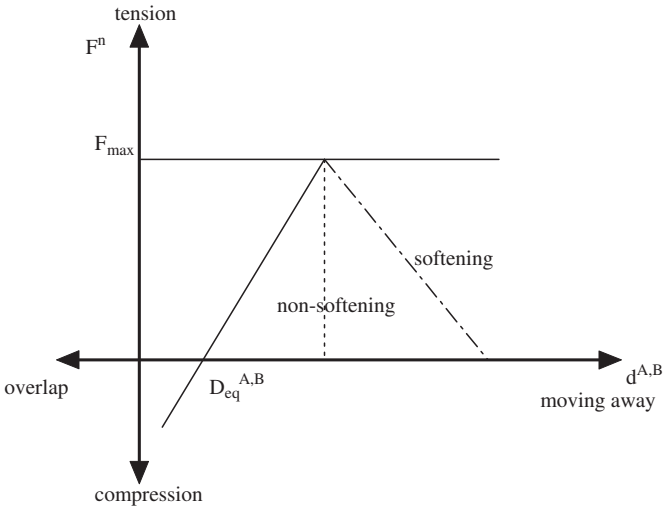

Fig. 3. Tensile failure criterion (modified after Donze [7]).

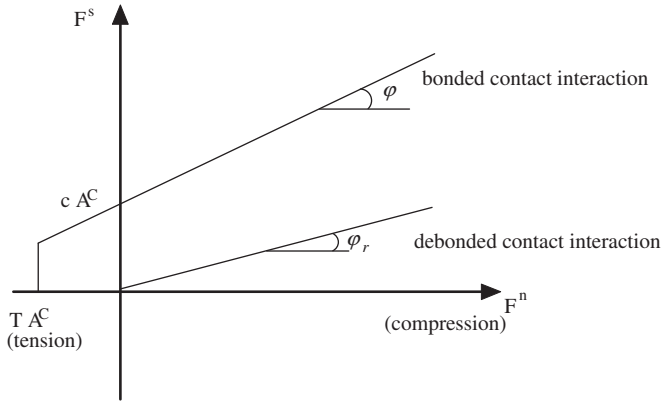

Fig. 4. Shear failure criterion (modified after Donze [7]).

as shown in Fig. 3, the contact force can gradually decrease rather than suddenly dropping to zero after the contact force reaches the peak value. In the work presented in this paper, softening behavior is not included.

The shear failure follows the Coulomb criterion as shown in Fig. 4. The maximum shear strength, τ_{max}, is dependent on cohesion c, friction angle φ and also normal stress, σ_n, at contact.

$$\tau_{max} = c + \sigma_n \tan\varphi. \tag{5}$$

After shear failure, the cohesion is set to zero and the frictional angle can decrease to residual frictional angle φ_r.

The micro-level parameters used to describe the contact strength, T, for tensile component and c, φ and φ_r for shear component are different from the values for material property at the macro level, and need to be identified by a calibration process. The effect of φ_r on the macroscopic behavior of simulated materials is mainly related to post-peak behavior rather than ultimate strength, which will be addressed in Section 5. Hence, φ_r was fixed as 30% of φ and it was not considered in the calibration process to match a failure envelope.

In the authors' model, contact bond is created by tensile strength and pressure dependent shear strength; bending stiffness is not included in the current model. Although bending stiffness is not introduced, rotation resistance between bonded particles still exists because shear force at contact contributed from particle rotation can resist the rotation.

3. Simulation setups

In order to calibrate the model, uniaxial compressive, triaxial compressive and direct tension tests, with a cylindrical specimen are simulated. Several techniques and algorithms developed for modeling these tests are presented here.

3.1. Membrane boundary for applying confining pressure

A new approach to apply realistic confining pressure has been developed for modeling triaxial tests on rock using the DEM. Currently, the conventional rigid boundary is commonly used in DEM simulations [6,16]. The drawback of this type of boundary condition is that the boundary particles tend to be aligned with the rigid boundary, and the material failure process and deformation may be overly constrained by the boundary, hence not fully representing the actual test conditions.

The new approach applies updated force boundary rather than a "wall" boundary to simulate the confining pressure. The applied forces only act on the boundary particles, which are identified and updated periodically. The boundary particles are identified by using a cell algorithm and updated frequently.

The force applied to an individual boundary particle is directly determined based on the applied confining pressure and the sphere size. After identifying the boundary particles, the effect of the confining pressure is simulated by applying force onto these boundary particles. The radial force applied on the ith individual boundary particle under membrane boundary condition, F_i^m, is determined based on the value of input confining pressure, p, and the radius of the particle, R_i, as

$$F_i^m = \pi R_i^2 \frac{A_b^m}{\sum_{i=1}^{i=N_b^m} \pi R_i^2} p, \tag{6}$$

where A_b^m is the initial lateral surface area of the specimen, and N_b^m is the number of boundary particles. The boundary force, F_i^m, is applied at the center of its relevant sphere, and is directed radially. The way to apply confining pressure is much realistic compared to other traditional approaches used in DEM modeling. However, one may argue that the full size of the sphere is used rather than the area of the sphere which is actually exposed to the surface when calculating boundary force, F_i^m. This is to compromise computational cost and accuracy because it is very computationally expensive to calculate particles' exact exposure to the surface.

Fig. 5 shows an example in which the boundary particles are identified after loading the specimen to failure with a packing of 2500 spheres. Notice that the specimen bulges at several locations, which cannot be modeled by using conventional rigid boundary conditions.

3.2. Simulation procedures

In modeling a triaxial test, the confining pressure is first applied to all boundary particles (all-around pressure) to reach an equilibrium state. Under this all-around confining pressure, the specimen develops a displacement at the top end of the specimen. Then an axial displacement is applied incrementally while keeping the confining pressure constant on circumferential boundary particles.

The starting point of the shearing phase for a triaxial test is simulated by applying an incremental displacement to the top end while the bottom end is fixed in the vertical direction like what behaves in actual triaxial experiments. Both the top and the bottom ends are treated as rigid walls. At each incremental step, the top-end displacement is increased by a certain amount, and this displacement is then kept constant until the system reaches equilibrium. When a displacement is applied to the top end, relatively large overlaps between the top end and the particles in contact with the top end are produced, and large stresses are applied to those particles. These stresses then propagate out into the specimen with relative movements among particle systems. The equilibrium state can be indicated by monitoring either the system energy history or the balances between the stresses applied at the two ends of the specimen. In the simulations carried out in this paper, the latter one was used to check the equilibrium state during a simulation. Displacement increment is increased if the relative difference of stresses calculated at the two ends of specimen is smaller than 1%. By monitoring the normal stress and strain in the axial direction, the stress–strain curve can be easily obtained, which is then used to analyze the macro material properties of the simulated specimen. The procedure for simulation of uniaxial test are similar to that for triaxial test except that the first step of applying confining pressure is not needed, and hence no membrane boundary is necessary.

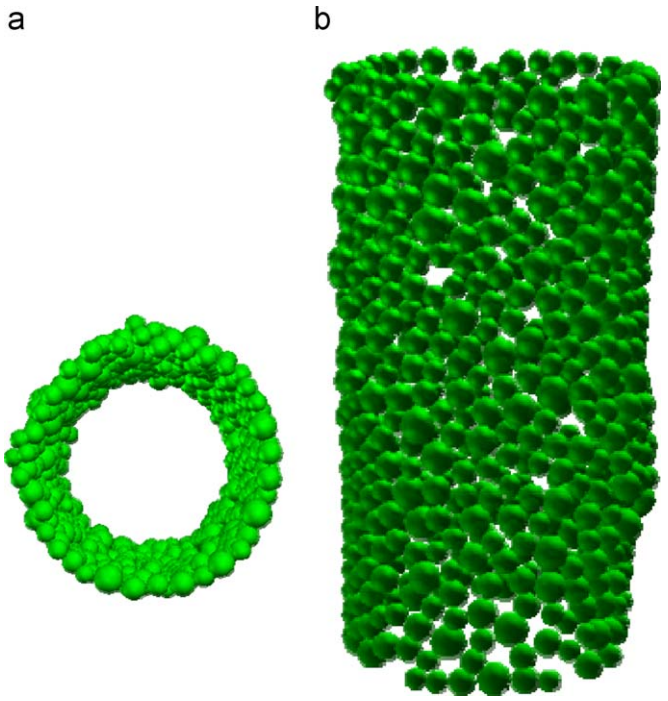

Fig. 5. Results of identified boundary particles for post-peak stage: (a) top view and (b) front view.

4. Model calibration

In order to simulate a specific problem, the micro parameters of the model described above should be calibrated to reproduce similar macro material properties as desired. There are two types of micro parameters to be determined in DEM, i.e., deformability and strength parameters. These micro parameters are calibrated with uniaxial and triaxial tests (axisymmetric).

In the calibration process, the experiment data of Lac du Bonnet granite published in [6,21] are used as presented in Table 1 to calibrate both deformability and strength parameters of the model.

A cylindrical specimen with a height of 3.2 and 1.6 cm diameter is prepared for calibration using a random packing of 2500 spheres as described in Section 3.1. The size of the specimen is the same as the one used in Hentz et al.'s work [7] for the purpose of comparison.

4.1. Deformability parameter identification

Deformability parameters include particle's Young's modulus, E_c, and the ratio of normal stiffness over shear stiffness at contact, K_s/K_n, where the contact normal stiffness is determined by $K_n = \pi E_c D_{eq}^{A,B}/4$. These micro deformability parameters are calibrated to match the material's macro deformability parameters: Young's modulus, E, and Poisson's ratio, ν, which are determined from experiments.

The identification of deformability parameters is carried out under non-failure condition by means of modeling uniaxial compressive tests. The average axial component of the stresses in the entire assembly can be determined either by the method of Liao (to determine the full stress tensor) [22] or simply by averaging the normal components of the contact forces on both the bottom and top ends (to obtain the axial stress). The two methods give comparable results (within a 15% difference), but the latter one is used because it more closely resembles the way in which stresses are calculated in a triaxial test.

As can be seen in Figs. 6 and 7, material's Young's modulus, E, is related to both particle's Young's modulus and the ratio K_s/K_n, while material's Poisson ratio ν is only related to the ratio K_s/K_n. When determining material's Young's modulus, E, particle's Young's modulus and the ratio K_s/K_n are independent of each other. This allows us to investigate this individual effect on E and then combine those effects together to determine material's Young's modulus E as follows.

Different combinations of E_c and K_s/K_n are used to set up a series of simulations for a given random packing. A sensitivity analysis is then carried out by varying one of the factors and fixing the other factor. As seen in Fig. 6, it is found that the material's macro Young's modulus, E, increases linearly with particle's Young's modulus, E_c, and the material's macro Poisson's ratio does not change with particle's Young's modulus, E_c. By fitting the simulation results (as shown in Figs. 8 and 9), the following relationships are obtained based on formulas presented by Liao [22]:

$$E = 2.43E_c\left(\frac{0.209 + 1.206\frac{K_s}{K_n}}{1 + 1.735\frac{K_s}{K_n}}\right), \tag{7}$$

$$\nu = 0.96\left(\frac{0.39 - 0.10\frac{K_s}{K_n}}{1 + 4.84\frac{K_s}{K_n}}\right). \tag{8}$$

Eqs. (7) and (8) can be solved for the micro deformability parameters for the model of Lac du Bonnet granite, which are found to be equal to $E_c = 104.7$ GPa and $K_s/K_n = 0.085$. With these model parameters, the simulated macro properties in deformability are as presented in Table 1 (third row, columns 2 and 3), which are very close to the experimental results.

The values of the coefficients in Eqs. (7) and (8) are valid only for a given packing assembly and initial contact relationships with a given coefficient of interaction range. For a different packing assembly, the forms of Eqs. (7) and (8) remain the same but the whole calibration procedure must be repeated because it is impossible to give a general formula to identify the micro parameters on the basis of the macro parameters.

Table 1
Macro-properties of Lac du Bonnet granite.

Property	E (Gpa)	ν	q_u (MPa)	φ (deg)	c (MPa)	σ_t (MPa)
Experimental	69	0.26	216	59	30	9.3
DEM model	71	0.25	220	58	32.6	19.1
PFC3D model	69.2	0.256	198.8	32.1	55.1	27.8

4.2. Strength parameter identification

There are two kinds of failure mechanisms, i.e. shear and tension, controlling the material failure. They can affect each other because either type of failures may change local stress conditions. This actually makes the failure process more complicated and makes it difficult to calibrate strength parameters. Strength parameters include the contact tensile strength, T, and c and φ

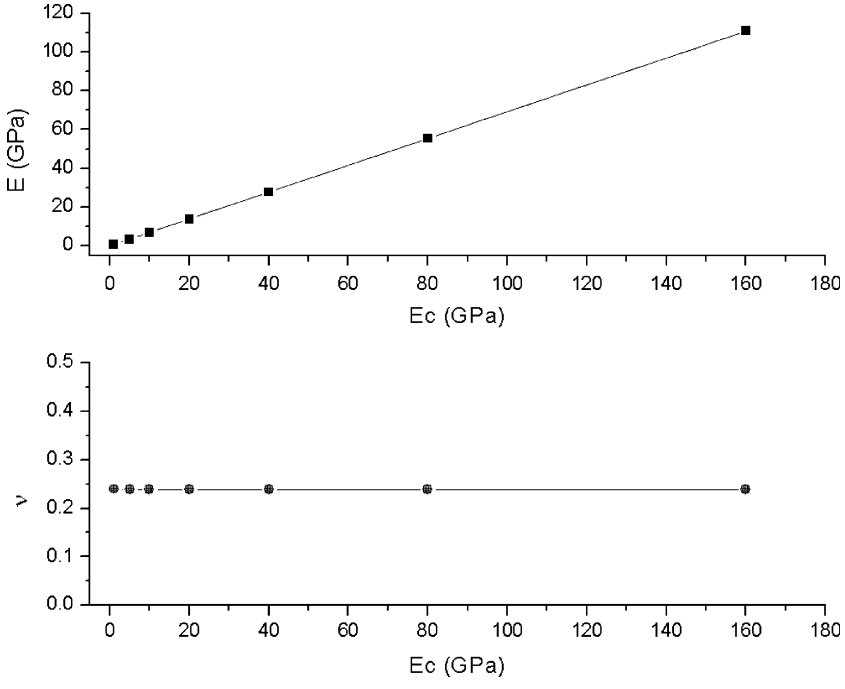

Fig. 6. Macro elastic properties vs. E_c.

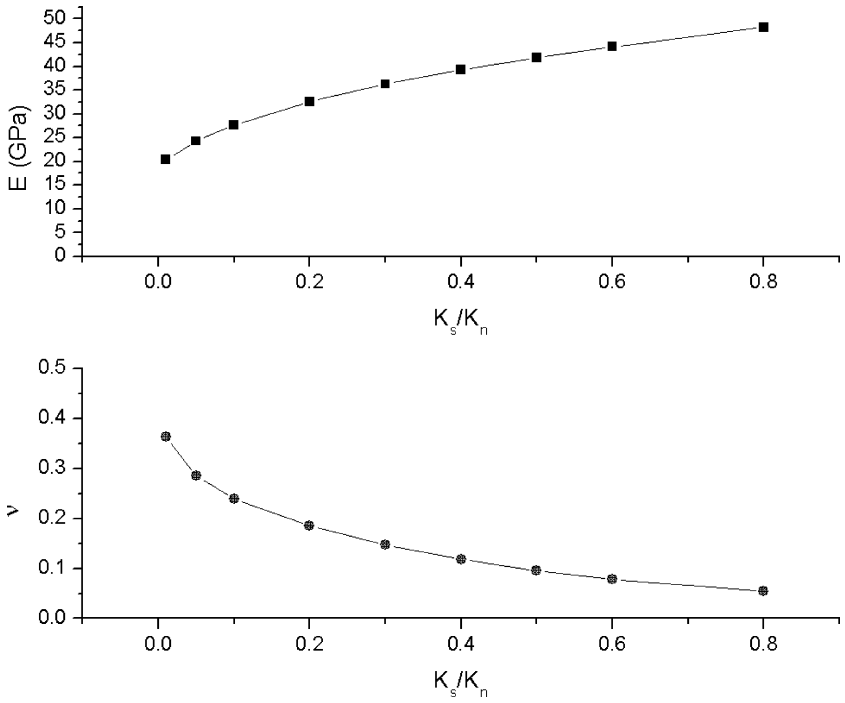

Fig. 7. Macro elastic properties vs. K_s/K_n.

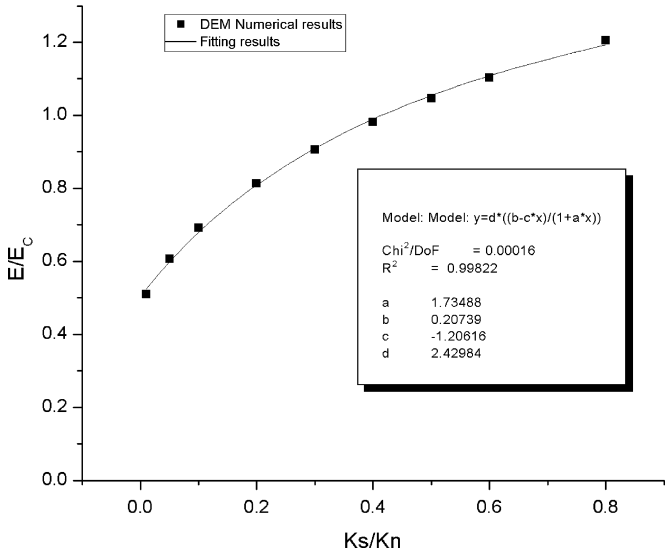

Fig. 8. Fitting results: material's Young's modulus vs. K_s/K_n.

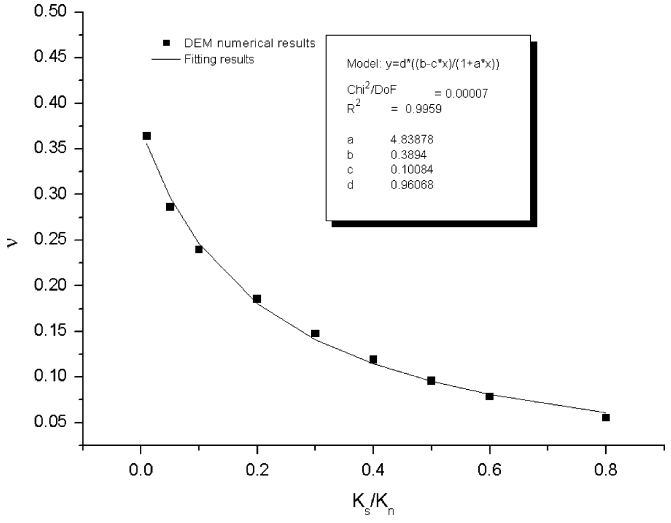

Fig. 9. Fitting results: material's Poisson's ratio vs. K_s/K_n.

for shear components as already described in the failure criteria of the model. These strength parameters are calibrated under different confining pressures to match a failure envelope obtained from experiments. This process is very time-consuming as each trial parameter set needs to be simulated under different confining pressures to reach the peak strength point of a stress–strain curve.

In order to rationally identify the strength parameters, an inverse method is used. The main objective of the inverse method used here is to identify a selected set of unknown modeling parameters in DEM to improve the agreement with experimental data. The experimental failure envelope is usually obtained by setting up a set of triaxial tests with different confining pressures to get the ultimate strength. In order to match the experimental failure envelope, some representative points, $(\sigma^i_{1\_\exp}, p^i)$, from the experimental failure envelope are selected to delineate the envelope, where $\sigma^i_{1\_\exp}$ is the ultimate axial strength under confining pressure p^i $(i = 1, 2, 3, \ldots, n)$, and n is the number of points chosen to describe the envelope. The corresponding confining pressures, p^i, are used for DEM simulation setup. For a given set of micro strength parameters, $[c, \varphi, T]$, the simulated ultimate strength under confining pressure p^i, is denoted as $\sigma^i_{1\_\mathrm{sim}}$. The objective function

$$f(c,\varphi,T) = \sqrt{\sum_{i=1}^{n}\left(\frac{\sigma^i_{1\_\exp} - \sigma^i_{1\_\mathrm{sim}}}{\sigma^i_{1\_\exp}}\right)^2} \tag{9}$$

is used to evaluate the difference between experimental and simulated failure envelopes.

The global optimization package SNOBFIT [23] was utilized in the calibration process, in which an optimization problem is

solved with objective function $f(X)$ subject to $X \in [U, V]$, where X is the parameters set, $[c, \varphi, T]$, to be identified, and $[U, V]$ is the parameter space, which is bounded by using specified ranges as

$$\begin{bmatrix} c_{low} & c_{up} \\ \varphi_{low} & \varphi_{up} \\ T_{low} & T_{up} \end{bmatrix}.$$

SNOBFIT performs global and local search by branching and local fits to find the global optimal point. This technique is especially suitable for optimizing problems with multiple local optimal points. In the calibration of strength parameters, the objective function in Eq. (9) is not available in an analytical form because a DEM code accounting for an intricate physical process is utilized to compute the failure envelope with specified micro strength parameters. SNOBFIT is the only global optimization code that handles non-analytical objective functions. The way in which the micro strength parameters affect the material strength is very complex, and the relationships of these strength parameters involved in determining the objective function, $f(c, \varphi, T)$, may not be monotonic. Our extensive numerical simulations have shown that SNOBFIT is able to optimize this complicated objective function to find the micro strength parameters.

At each step of the optimization process, SNOBFIT generates a specified number of evaluation points, and then proceeds by successively partitioning the parameter space and building local quadratic models of the objective function. The search process is terminated when a given minimal objective function value is reached or if no better solution can be found after a specified number of steps [23]. Compared to typical stochastic algorithms, SNOBFIT does not require as many function evaluations and is therefore applicable to problems with expensive function evaluations, such as DEM to obtain a failure envelope.

The overall calibration procedure proceeds iteratively. With reference to Fig. 10, one starts from either an initial guess of model parameters or parameter values randomly chosen from specified ranges of values. Then, the unknown parameters X are iteratively updated to find the optimized parameters X: at the ith iteration, the DEM code is invoked to obtain a computed failure envelope (CFE) corresponding to parameters X^i. The CEF is then compared to the experimental failure envelope (EFE) to evaluate the objective function $f(c, \varphi, T)$. If the value of objective function is smaller than the given tolerance, optimized model parameters will be outputted. Otherwise, the model parameters are updated by calling SNOBFIT. In the calibration process, the DEM code and SNOBFIT were repeatedly invoked until CFE matches EFE by meeting the tolerance criterion, which was set as 5% in the

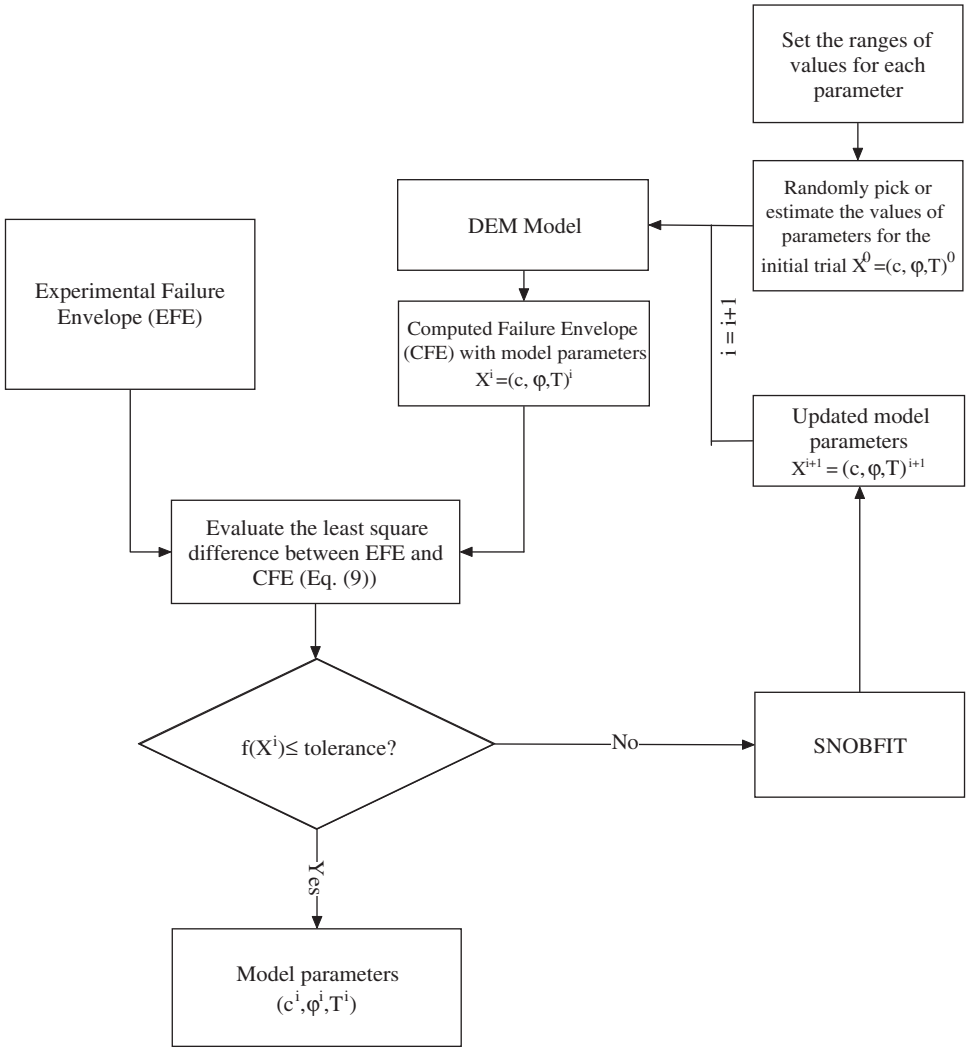

Fig. 10. Flowchart of the inverse method for strength parameters identification.

strength parameters calibration considering the intensive computational effort involved in obtaining the value of objective function. In the calibration work presented in this paper,

$$\begin{bmatrix} c_{low} & c_{up} \\ \varphi_{low} & \varphi_{up} \\ T_{low} & T_{up} \end{bmatrix} = \begin{bmatrix} 20\,\text{MPa} & 1000\,\text{MPa} \\ 0^\circ & 80^\circ \\ 5\,\text{MPa} & 100\,\text{MPa} \end{bmatrix}$$

is used for the parameter ranges for Lac du Bonnet granite, which are roughly estimated based on available experimental strength data. The number of points, n, chosen to delineate the failure envelope is 6.

All the simulations for strength parameter calibration use the deformability parameters identified in Section 4.1 and Table 1. The calibrated micro strength parameters are $c = 429\,\text{MPa}$, $\varphi = 68^\circ$ and $T = 34.2\,\text{MPa}$. The calibrated failure envelopes are shown in Fig. 11, which shows that the simulated envelope with calibrated micro strength parameters matches well the experimental one. The results demonstrate a prominent pressure-dependent behavior compared to PFC model results [6] (Table 1 and Fig. 12). A total number of 95 iterations are necessary to find the calibrated micro strength parameters with a tolerance criterion of 5%, i.e. 95 failure envelopes are generated, each corresponding to different strength parameter combinations.

The corresponding stress–strain curves under different confining pressures are plotted in Fig. 12; they show that all curves have the same slope (Young's modulus), and that specimens under higher confining pressure fail at larger strain and under higher deviator stress ($(\sigma_1 - \sigma_3)_{\text{at failure}}$).

It should be noted that the calibrated values of micro strength parameters in DEM model are different from the ones at macroscopic level. In DEM modeling, failure either in tension or shear is initiated from those highly stressed contact bonds and propagates subsequently. Hence, calibrated micro strength parameters could be much higher than effective strengths, as can be seen from the strength parameter calibration of Lac du Bonnet granite, in which the calibrated model strength parameters c, φ and T are all much higher than macroscopic ones as shown in Table 1.

4.3. Discussions on model calibration

Unlike other numerical methods such as finite element method, in which model parameters can be directly derived from experimental results, DEM deformability and strength parameters used at the micro level are different from the material properties at the macro level. That is why special calibration algorithms were proposed. In DEM modeling, specimens are prepared by random sphere packing. Different packings have different internal structures even for the same number particles. These internal packing structures can affect the macroscopic behavior of packing assemblies. As a result, in DEM modeling, every packing specimen must be calibrated by using the algorithms discussed above to

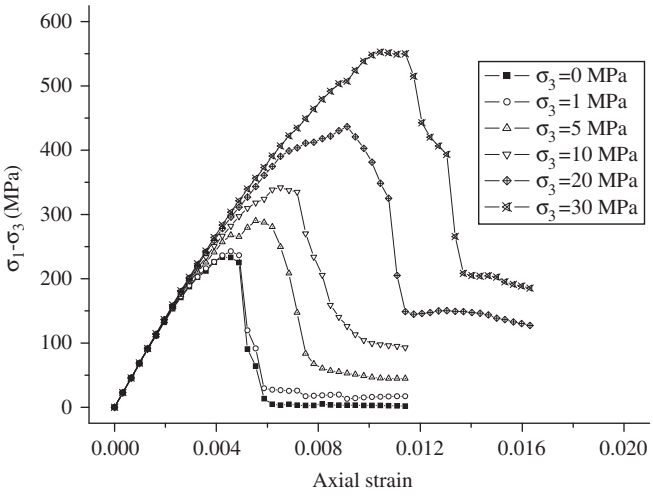

Fig. 12. Stress–strain curves for different confining pressure.

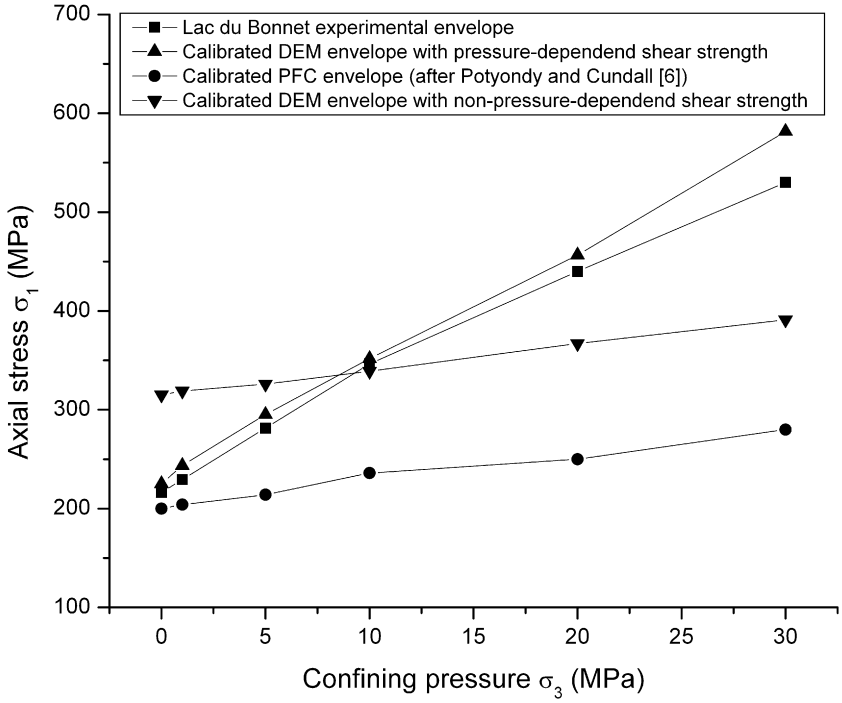

Fig. 11. Strength parameters identification results.

match the desired properties before using it in actual simulations. Usually, different packings should have different micro model parameters to match specific material properties.

PFC's bonded particle model (BPM) [6] is often used to model intact rock behavior. However, if clusters of spheres are not used, BPM has difficulty in modeling the behavior of Lac du Bonnet granite, which has a high slope strength envelope, and a high ratio of compressive strength to tensile strength as shown in Fig. 11. Potyondy and Cundall [6] concluded that: "this discrepancy may arise from the use of circular and spherical grains in the present model, and it could be reduced by using grain shapes that more closely resemble the complex-shaped and highly interlocked crystalline grains in granite." When using clusters of spheres, a good match with experimental envelope slope was obtained, but other problems, like discrepancy in dilation and post-peak behavior, were observed. After an effective calibration, the model presented in this paper can reproduce the behavior of Lac du Bonnet granite. Unlike the authors' model, the micro shear strength in BPM model is not pressure-dependent (it only includes cohesion), which might cause the difficulty in modeling a high strength envelope slope (macro internal frictional angle).

In order to understand the importance of pressure-dependent shear strength in simulating a high strength envelope slope, a DEM model with a non-pressure-dependent shear strength ($\varphi = 0$ in Eq. (5)) was calibrated against the experimental data of Lac du Bonnet granite. The values of micro deformability parameters are the same as those identified previously. Now only two parameters are involved in strength parameter identification, i.e., c, and T.

The optimum result obtained after 100 iterations has strength parameters equal to $c = 239$ MPa, and $T = 47$ MPa and its failure envelope is shown in Fig. 11 (failure envelope for non-pressure-dependent shear strength). It shows that the Lac du Bonnet granite experimental failure envelope cannot be modeled by only using model strength parameters c and T. This model is still different from PFC's BPM model because of the concepts of equilibrium distance and interaction range used in the model, therefore the identified model strength parameters cannot be directly compared to those used in the BPM model. It is concluded that pressure dependent micro shear strength is critical to correctly simulate high slope failure envelopes.

4.4. Simulation of direct tension test

In practice, Brazilian test is usually carried out to determine the material tensile strength. However the strength parameters calibrated from triaxial tests to determine material tensile strength cannot be directly used to model Brazilian test. Because the packing assembly used for Brazilian test (disk) is different from packing assembly used for triaxial test (cylinder), the calibrated strength parameters for the triaxial test specimen may not be suitable for a disk specimen any more.

From a numerical point of view, a direct tension test can be easily set up to determine tensile strength. With the calibrated strength parameters, a direct tension test is simulated by applying incremental tensile displacement loading. The tensile strength between specimen ends and loading platens (interface) are set high enough to make sure that no failure can occur at the interface. As shown in Fig. 13, the simulated tensile strength is about 19.1 MPa (for mean particle radius of 0.70 mm), which is higher than the experimental value of 9.3 MPa obtained from Brazilian tests. The tensile strength simulated by PFC3D in Potyondy's work [6] was about 28 MPa. The difference in the simulated tensile strength may be caused by different reasons. First, the model used in this work is different from PFC's BPM in several ways, such as concepts of equilibrium distance and interaction range, and pressure-dependent shear strength. Further, Potyondy and Cundall used different specimens for simulating triaxial and Brazilian tests, and hence the internal packing structures were different. As highlighted in this paper, in order to model a specified material, different packing structures should have different micro model parameters. However, Potyondy and Cundall adopted the model parameters identified by using uniaxial tests even in modeling Brazilian tests. Lastly, the tensile strength obtained from Brazilian tests is normally higher than that obtained from direct tension tests because Brazilian tests induce a biaxial state of stress, in which some micro cracks may be due to compressive load under the loading platens. Usually, it is difficult to fully model a material behavior with very high ratio of uniaxial compressive strength over tensile strength. However, the ratio of uniaxial compressive strength to tensile strength of about 12 obtained here is a representative value for intact rock material.

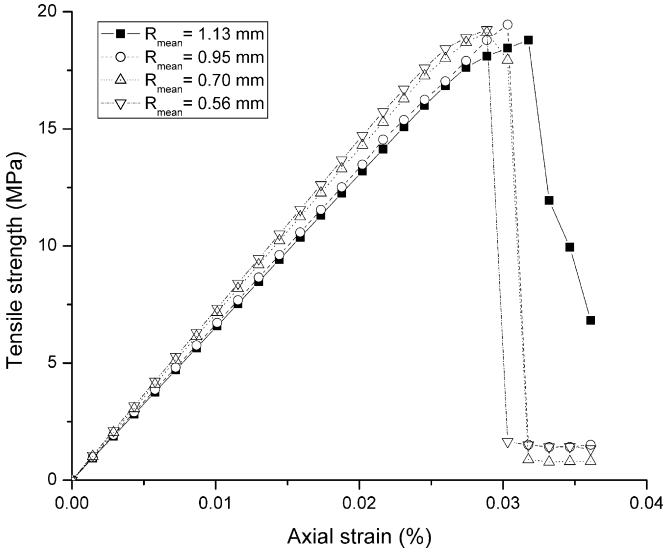

Fig. 13. Stress–strain curves for direct tension test.

4.5. Effect of internal packing structure on macro properties

The effect of internal packing structures on macro material properties is investigated in this section in terms of particle size and random process in packing. The investigation demonstrates that internal packing structure is an intrinsic part of material characterization in discrete element modeling.

First, packing assemblies were performed with different mean particle sizes while keeping all other micro parameters fixed. The mean particle radii for the five different packing assemblies are 0.44, 0.56, 0.70, 0.95, and 1.13 mm, respectively. Simulated results show that the particle size can affect macro properties in both deformability and strength. Poisson's ratio is independent of particle size, while Young's modulus exhibits a clear dependency upon particle size because it decreases from 75.1 to 65.2 GPa as particle size increases from 0.56 to 1.13 mm (Fig. 14a). The reason for this dependence is unknown, but it should be related to the internal structure of the random packing because such dependence is not observed while using regular packings, in which spheres are all the same size and face centered. Figs. 13 and 14b that the simulated uniaxial unconfined compressive strength and tensile strength exhibit no clear increasing or decreasing trends with particle size.

Different random processes in packing can also cause changes in internal packing structures. A set of triaxial

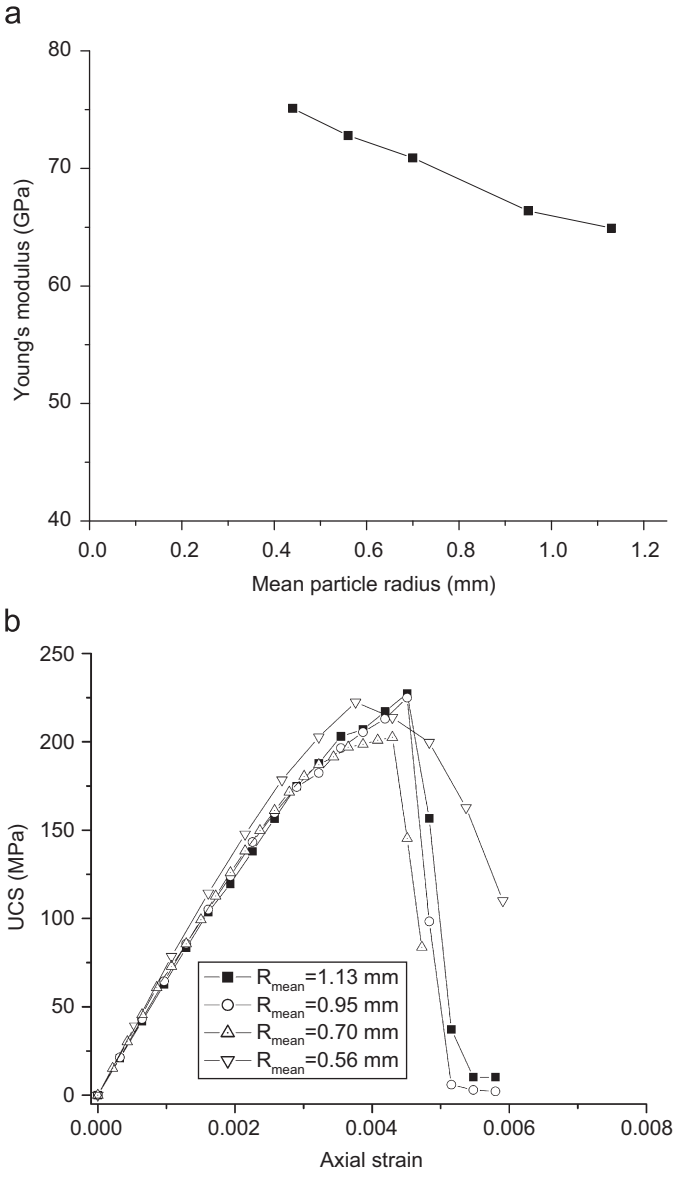

Fig. 14. Effect of particle size on simulated macro properties: (a) dependence of Young's modulus on particle size and (b) stress–strain curves for different mean particle sizes.

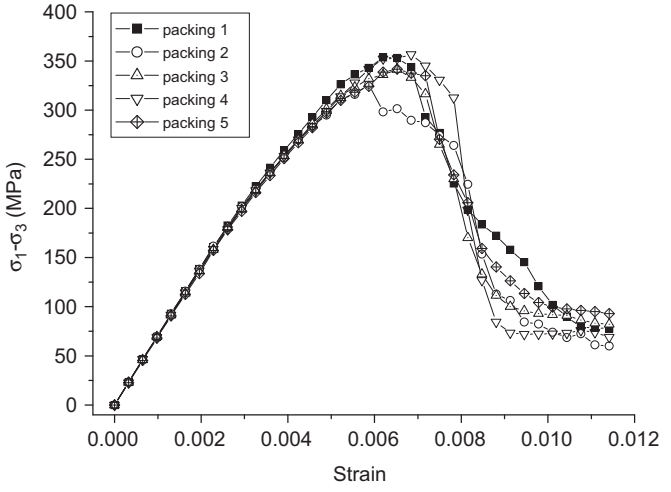

Fig. 15. Effect of random distribution of particles on material behavior.

simulations ($\sigma_3 = 10$ MPa) were performed with packing assemblies generated by different random processes while using the same type of particle sizes. Fig. 15 shows that the difference in ultimate deviator stress ($(\sigma_1 - \sigma_3)_{\text{at failure}}$) can be as large as 15%. However, this random process has negligible effect on Young's modulus and Poisson's ratio.

In conclusion, internal packing structures can affect macro material properties even if all micro-properties are kept constant, and have to be taken into account in model calibration.

5. Crack evolution

The macro failure of the material is caused by the evolution and propagation of local cracks which can be identified by the history of the number of contact failures (cracks). When a specimen fails in the simulation, a failure zone forms, which is either a shear plane for triaxial test or a tensile failure section. Along these failure zones, contacts are broken apart by tensile failure cracks and particles are rearranged. For triaxial compressive tests, the stress–strain curve can be classified into three distinct stages as can be seen in Fig. 16 based on the generated cracks described as follows:

Stage I: Very few cracks are generated and the material behaves elastically.
Stage II: Tensile cracks are gradually generated over a strain-loading increment; cohesion component of the cracked contact is also destroyed, and the material behaves plastically.
Stage III: The frictional strength (residual contact shear strength) starts to mobilize gradually until reaching the residual shear strength of the material along a shear band, which is made up by those particle contacts firstly broken by tensile failure followed by loss of cohesion in the shear strength at contact. In this stage, the newly generated contact failures in tension are very few because the additional strain mainly takes place in the shear band, which is formed by broken contacts. This stage characterizes the post-peak behavior of compression test.

When the loading increases, the cohesion component of shear strength is gradually destroyed by tensile cracking. The normal stress-dependent frictional strength (residual shear strength at contact) is only mobilized after the specimen reaches macro failure (peak strength), when the cohesional component of shear strength is significantly reduced, and the rock fragments can move

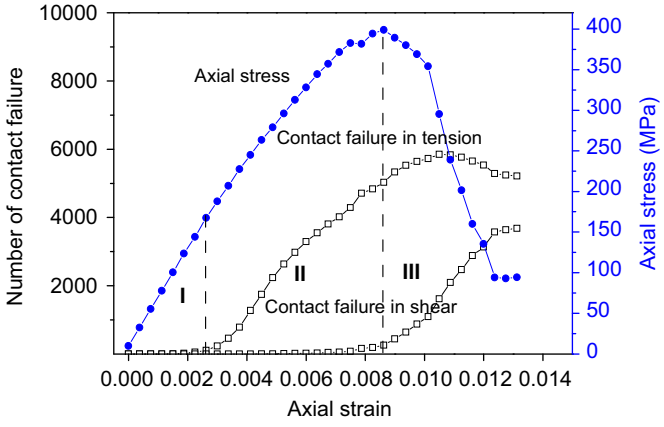

Fig. 16. History of contact failures during triaxial compressive test.

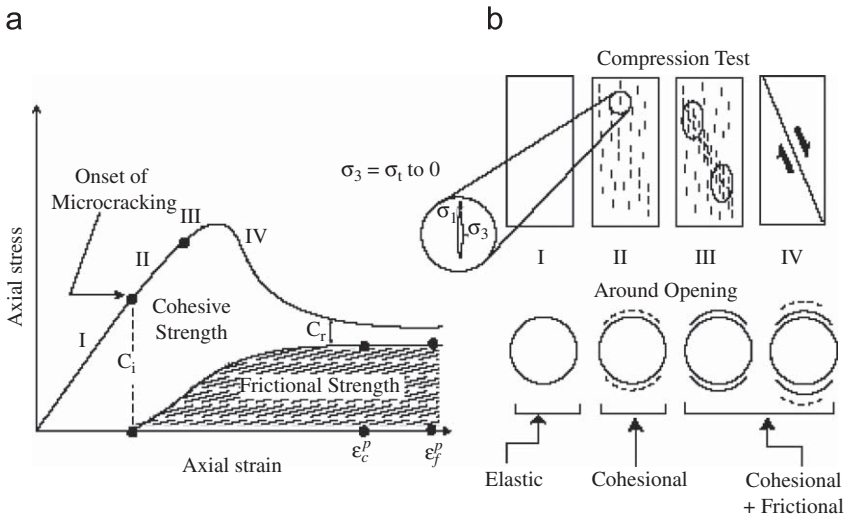

Fig. 17. Mobilization of the strength components (after Ref. [5]).

relative to each other in shear. In other words, the residual frictional strength at contact (micro level) only affects the post-peak behavior for brittle materials.

The results of failure process for compression test shown in Fig. 14 can be compared with the investigations made in [5, 736, Fig. 10] (as shown in Fig. 17), in which Hajiabdolmajid et al. concluded that, in relatively low confinement environments, the delay in frictional strength mobilization is characteristic of brittle failure in geomaterials. Based on the authors' investigations, the micro tensile strength at contact dominates the strength before brittle failure. When the loading increases, the cohesion component of shear strength is gradually destroyed by tensile cracking as shown in Fig. 16. The normal stress-dependent frictional strength (residual shear strength at contact) is only mobilized after the specimen reaches macro failure (peak strength), when the cohesion component of strength is significantly reduced, and the rock fragments can move relative to each other in shear. In other words, the residual frictional strength at contact (micro level) only affects the post-peak behavior for brittle materials, like Lac du Bonnet granite.

6. Conclusions

Other than using some traditional approaches to identify micro model parameters in DEM modeling, a special calibration scheme has been developed. Sensitivity analysis is used to identify micro deformability parameters by obtaining relationships between microscopic and macroscopic deformability properties. Micro strength parameters are identified by a global optimization process aimed at minimizing the difference between computed and experimental failure envelopes. With these identification algorithms, the model has been successfully calibrated to match experimental triaxial test data of Lac du Bonnet granite. These calibration algorithms can be applied to identification of micro model parameters for any type of DEM code.

Investigation on failure evolution of simulated Lac du Bonnet granite is then performed. The monitored evolution of the number and type of contact failures (micro cracks) reveals that at micro level tensile failures occur first followed by mobilization of residual friction, and that three distinct stages of stress–strain curve can be well represented by the accumulated number of contact failures and the mode of contact failures.

Acknowledgment

The authors are grateful to Rio Tinto for sponsoring this research work under the project "Three-dimensional rock-fall analysis with impact fragmentation and fly-rock modeling".

References

[1] Hoek E. Strength of jointed rock masses. Géotechnique 1983;23(3):187–223.
[2] Cundall PA, Hart HR. Numerical modeling of discontinua. Journal of Engineering and Computer 1992;9:101–13.
[3] Cundall PA, Strack ODL. A discrete element model for granular assemblies. Geotechnique 1979;29(1):47–65.
[4] Cundall P. A computer model for simulating progressive large scale movements in blocky rock systems. In: Proceedings of the symposium of international society of rock mechanics, vol. 1. Nancy, France, 1971. Paper no. II-8.
[5] Hajiabdolmajid V, Kaiser PK, Martin CD. Modelling brittle failure of rock. International Journal of Rock Mechanics and Mining Sciences 2002;39(6):731–41.
[6] Potyondy DO, Cundall PA. A bonded-particle model for rock. International Journal of Rock Mechanics and Mining Sciences 2004;41(8):1329–64.
[7] Hentz S, Daudeville L, Donze F. Identification and validation of a discrete element model for concrete. Journal of Engineering Mechanics 2004;130(6):709–19.
[8] Cook B, Lee M, DiGiovanni A, Bronowski D, Perkins E, Williams J. Discrete element modeling applied to laboratory simulation of near-wellbore mechanics. International Journal of Geomechanics 2004;4(1):19–27.
[9] Ng T-T. Input parameters of discrete element methods. Journal of Engineering Mechanics 2006;132(7):723–9.
[10] Onate E, Rojek J. Combination of discrete element and finite element methods for dynamic analysis of geomechanics problems. Computer Methods in Applied Mechanics and Engineering 2004;193(27–29):3087–128.
[11] Donze FV, Bouchez J, Magnier SA. Modeling fractures in rock blasting. International Journal of Rock Mechanics and Mining Sciences 1997;34(8):1153–63.
[12] Cho N, Martin CD, Sego DC. A clumped particle model for rock. International Journal of Rock Mechanics and Mining Sciences 2007;44(7):997–1010.
[13] Schöpfer M, Abes PJ, Childs C, Walsh JJ, et al. The impact of porosity and crack density on the elasticity, strength and friction of cohesive granular materials: insights from DEM modelling. International Journal of Rock Mechanics and Mining Sciences 2009;46(2):250–61.
[14] Yoon J. Application of experimental design and optimization to PFC model calibration in uniaxial compression simulation. International Journal of Rock Mechanics and Mining Sciences 2007;44(6):871–89.
[15] Fakhimi A, Villegas T. Application of dimensional analysis in calibration of a discrete element model for rock deformation and fracture. Rock Mechanics and Rock Engineering 2007;40(2):193–211.
[16] Itasca. PFC3D Manual, 1st ed.; 1999.
[17] Richard P, Jensen PJB, Michael EP, Tuncer BE. DEM simulation of granular media–structure interface: effects of surface roughness and particle shape. International Journal for Numerical and Analytical Methods in Geomechanics 1999;23(6):531–47.

[18] Kuhn MR. A flexible boundary for three-dimensional DEM particle assemblies. Engineering Computations 1995;12(2):175–83.
[19] Wang Y, Tonon F. A new membrane boundary for DEM modeling of triaxial tests on intact rock. Journal of Engineering Mechanics 2009, in press.
[20] Wang Y, Tonon F. Calibration of a discrete element model for intact rock. International Journal for Numerical and Analytical Methods in Geomechanics 2009, in press.
[21] Martin C. The strength of massive Lac Du Bonnet granite around underground openings. PhD thesis, University of Manitoba, Winnipeg, Canada; 1993.
[22] Liao C, Chang T, Young D, Chang C. Stress–strain relationship for granular materials based on the hypothesis of best fit. International Journal of Solids and Structures 1997;34(31–32):4087–100.
[23] Neumaier A, Huyer W. SNOBFIT—stable noisy optimization by branch and fit. ACM Transactions on Mathematical Software 2008;35(2) p. article 9.